Calorimetric Measurement of Droplet Temperature in GMAW

Droplet temperature reaches a minimum at the transition from globular to spray transfer

BY E. J. SODERSTROM, K. M. SCOTT, AND P. F. MENDEZ

ABSTRACT

Average temperature was calculated from calorimetric measurements in free-flight gas metal arc welding (GMAW) for ER70S-6 (carbon steel), ER316L (stainless steel), and ER4030 (aluminum) electrodes. Measurements were conducted using a constant-pressure water calorimeter to capture the droplets and a flow-through copper cathode/calorimeter to carry the arc. Thermocouples were used to monitor the temperature change of the water flowing through the cathode as well as in the constant pressure calorimeter. Results show a local minimum in temperature during the transition from globular to spray transfer modes.

Introduction

Droplet temperatures during free-flight gas metal arc welding (GMAW) have been studied by several researchers. However, there is an incomplete understanding as to how droplet temperature is affected by process parameters. Understanding the response of droplet temperature with different transfer modes is necessary to understand fume formation rates and alloy recovery.

Droplet temperature measurements have been made using different methods, including thermocouples, optical pyrometry, and calorimetry (Ref. 1). Previous researchers have reported droplet temperatures ranging from the boiling point of the metal in question to several hundred degrees above the melting temperature (Refs. 2–7). Lu and Kou (Ref. 6) utilized a setup that implemented a gas tungsten arc welding (GTAW) torch to melt welding wire to simulate globular transfer and used a water-cooled copper cathode during spray transfer. In each case, the droplets were collected in a calorimeter surrounded by a radiation baffle. Ozawa et al. (Ref. 8) used a calorimeter setup similar to Lu's for droplet heat content measurements. The arc was established between a consumable anode and nonconsumable cathode using a variety of materials. Fu, Ushio, and Matsuda (Ref. 9) tested heat content of steel and aluminum alloys and analyzed the contributions of ohmic heating and heat input from the arc using a setup similar to Lu and Kou but with a carbon cathode. Attempts to acquire the droplets and measure heat content have also been made by Kiyohara, Yamamoto, and Harada (Ref. 10); Ando and Nishiguchi (Ref. 11); Acinger, Sipek, and Smars (Ref. 2); Erohin and Rykalin (Ref. 12); Watkins (Ref. 13); Pokhodnya and Suptel (Refs. 4, 14); Heiro and North (Ref. 15); Ueguri et al. (Ref. 16); and Tong et al. (Ref. 17).

In addition to measuring droplet temperatures, this setup also has the ability to separate heat generated by the arc from that contained within the droplets. The latest data from setups with similar capabilities are from the late 1980s, and the intervals of welding current used in surveying the process were coarse and insufficient to resolve the local minimum in droplet temperature reported in this work. Therefore, it is necessary to revisit the problem using an experimental matrix with slight variations of welding current. The scope of this project is limited to direct current electrode positive (DCEP) welding conditions with 1.1-mm (0.045-in.) ER70S-6 (carbon steel), ER4043 (aluminum), and ER316L (stainless steel) electrodes shielded with argon. Programmable waveforms and/or pulsing were not utilized in the study to minimize the number of experimental degrees of freedom. Although the switch to pulsing or a complex waveform is only a matter of changing the machine settings, the fundamental changes in droplet temperature are expected to be more complex than in direct current and outside the scope of this initial work. The following section describes the experimental setup in detail. The procedure implemented is found in Appendix C.

KEYWORDS

Gas Metal Arc Welding (GMAW)
Droplet Temperature
Globular Transfer
Spray Transfer
Stainless Steel
Aluminum

Experimental Setup

The experimental setup can be divided into six critical subassemblies. The welding equipment, calorimeter, copper heat shield, water-cooled copper cathode, high-speed imaging, and current/voltage data acquisition work simultaneously to provide feedback about the process.

Welding Equipment

The power source used in this research was a Miller PipePro 450RFC machine operated in constant voltage mode. Coupled to the power source was a Miller PipePro Single Feeder that communicated directly with the power supply for precise process control. The welding torch was a Miller Type GW-60A. An adapter was manufactured to allow for the use of the Miller Type GA-17C contact tip. An Omega gas proportioning rotameter Model FL-2GP-40ST-40ST was used for monitoring the flow rate of the shielding gas, received from the factory calibrated with a precision of ± 2%.

Calorimeter

Instrumental to the experimental setup was a constant-pressure calorimeter shielded from arc influence by a copper

E. J. SODERSTROM (esoderstrom@elwd.com) *is a metallurgical engineer, Ellwood National Crankshaft, Irvine, Pa. K. M. SCOTT* (kmscott@ualberta.ca) *is a graduate student and P. F. MENDEZ* (pmendez@ualberta.ca) *is associate professor, Weldco/Industry Chair in Welding and Joining, Canadian Centre for Welding and Joining, Department of Chemical and Materials Engineering, University of Alberta, Edmonton, AB, Canada.*

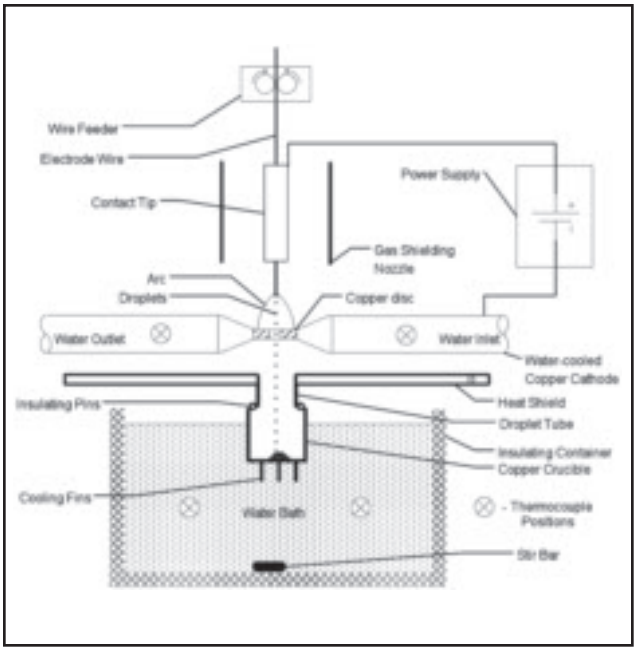

Fig. 1 — The experimental system. Droplets fall through the cathode and are captured in a copper crucible. The temperature change of the water bath is monitored with thermocouples. Not to scale (Ref. 18).

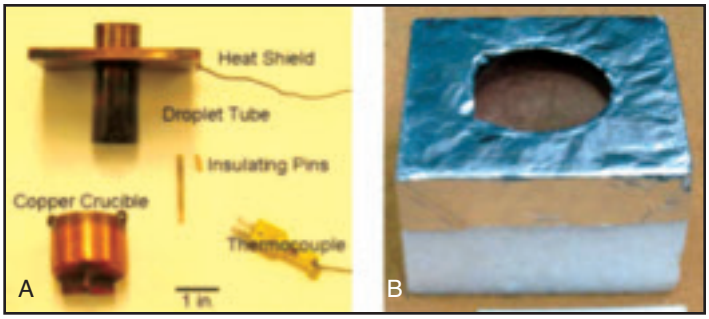

Fig. 2 — A — Components that facilitate capturing the droplets; B — constant-pressure calorimeter made from Styrofoam™ (Ref. 18).

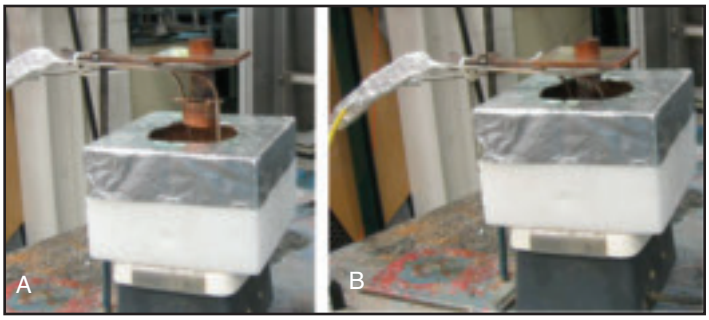

Fig. 3 — A —The assembled calorimeter. The crucible is elevated above the water bath to allow for the photograph; B — the crucible is submerged in the water bath during testing (Ref. 18).

plate along with a water-cooled copper cathode, shown in Fig. 1 (Ref. 18). Due to the harsh nature of the welding environment, many design issues had to be evaluated for feasibility. The first step in the design process was to identify the functionality of each component. After the design and fabrication of the experimental apparatus, a series of tests was performed to validate the system and verify all the components worked properly.

The function of the calorimeter was for the measurement of droplet heat content. Figure 1 shows the main components of the calorimeter system. It is composed of a water bath within an insulating container, a copper crucible to catch the droplets, a supporting system to hold the crucible, a stir bar to circulate the water, and thermocouples to measure the temperature or the water bath.

Figure 2 shows the two main components of the calorimeter, the "hot" components that experience elevated temperature during testing and the insulating container that holds the water bath. When assembled with the insulating pins, which are hollow alumina tubes, the copper crucible is thermally isolated from the droplet tube and heat shield. All of these parts fit together along with the thermocouples, magnetic stir bar, water, and stir plate to form the calorimeter, shown completely assembled in Fig. 3.

The process of acquiring temperature data proved to be difficult due to arc interference that affected data acquisition. Electrical noise greatly influenced the voltage output of the DAQ board. The problem could be solved by using low-noise thermocouples, Omega Model GKQSS-18U-18, as well as oversampling the data. This eliminated excess electrical noise to produce temperature profiles with negligible arc interference.

Copper Heat Shield

The calorimeter may be influenced by the plasma flame that is expelled through the disk of the calorimeter as well as additional radiation from the arc due to the proximity to the copper cathode. To account for this, a heat shield with an embedded K-type thermocouple was integrated between the calorimeter and cathode, as shown in Figs. 1 and 2. The shield can capture some of the radiative heating of the arc. The thermocouple does not account for temperature gradients within the heat shield during the duration of testing.

Water-Cooled Copper Cathode

The water-cooled copper cathode serves several purposes in the system. The first is to sustain the welding arc between itself and the consumable electrode, as shown by the circuit in Fig. 1. The second purpose is to allow passage of the detached droplets into the copper crucible. The third purpose is to monitor the temperature rise in the cooling water to determine the amount of heat that is supplied by the arc to the cathode.

The copper cathode assembly is shown in Fig. 4. Process water from the building's closed-loop system was used as the coolant. Ahead of the water inlet is a 0.2 to 2 gal/min flow meter indicating the flow rate of the process water. The volumetric flow rate is one of the terms needed to calculate the power being supplied to the cathode. The second value is the change in water temperature, which is monitored by the thermocouples placed in the flow-through ports.

Several cathode designs were tested to establish which would perform best for the duration of the study. Figure 5 shows a schematic representation of each. Version 1 is simply a section of 19.05 mm (0.75 in.) copper tubing with a through-hole drilled through the tube body. A smaller section of copper tube was brazed in place to provide a water-tight seal and a passage for the droplets. This design proved to be quite fragile and not sustainable; the arc wandered down the droplet passage and eventually extinguished. Variation 2 is similar to 1 but with a Mullite insulator pressed in place to keep the arc from wandering. This iteration also proved to be unstable, as the insulator melted in conjunction with establishment of the arc. Version 3 implemented a 25.4-mm- (1-in.-) diameter copper disk with a 0.925-mm (0.375-in.) through-hole that was brazed into 19.05-mm (0.75-in.) tubing that had been compressed. After compression, the di-

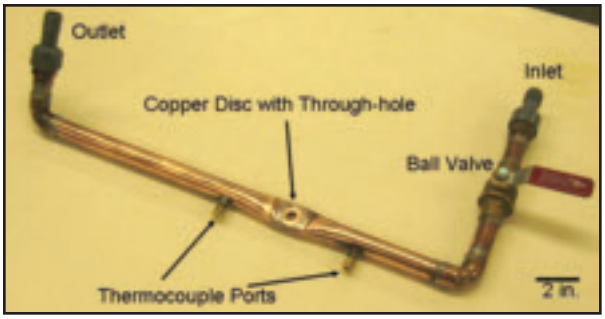

Fig. 4 — The water-cooled copper cathode. This piece of equipment acts to monitor water temperature before and after the arc and to allow droplets to travel unobstructed into the crucible (Ref. 18).

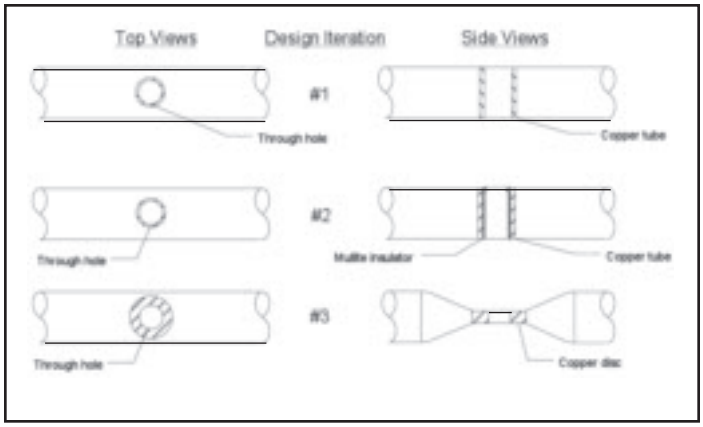

Fig. 5 — Copper cathode design iterations. Version 3 led to the most desirable arc characteristics (Ref. 18).

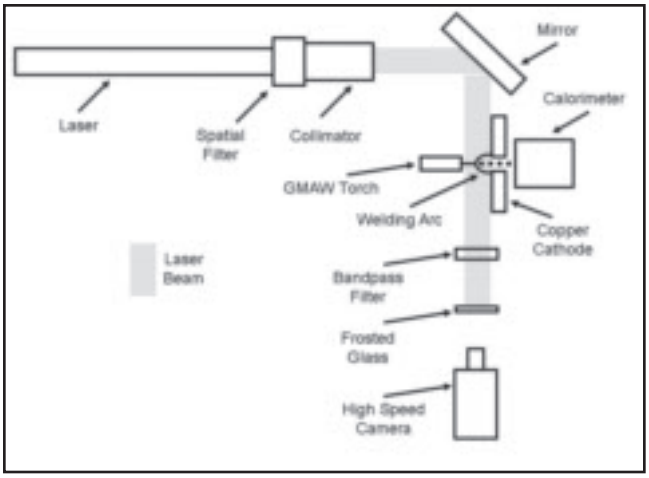

Fig. 6 — A schematic of the laser imaging system used in the research. The welding gun, calorimeter, and cathode have been rotated for the sake of the schematic. Actual welding position was vertical (Ref. 18).

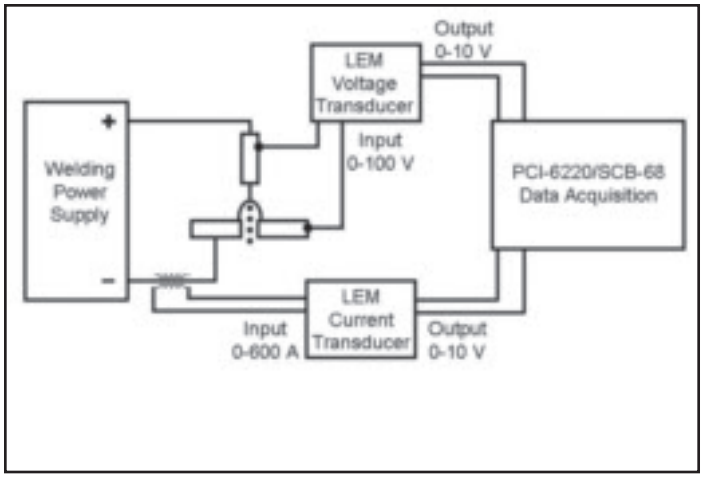

Fig. 7 — Diagram of the current/voltage data acquisition setup (Ref. 18).

mensions of the cathode at the copper disk were 31.75 mm wide × 6.35 mm thick (1.25 in. × 0.25 in.). The flat surface of the disk allowed the arc to be established and maintained consistently resulting in an arc that is typical of standard bead-on-plate GMA welds. Although undocumented, arc stability on the copper cathode will be demonstrated in subsequent publications. The consistent results led to the implementation of this version for the remaining tests.

Imaging System

This setup is very similar to the laser shadowgraph system used by Allemand et al. (Ref. 19), which has seen wide use by many researchers and is shown in Fig. 6.

The high-speed camera used in this research was an X-PRI model manufactured by AOS Technologies AG. Recordings were made at either 1000 or 2000 frames per second, depending on the metal transfer mode. The lens used for imaging was a variable zoom (0.5 to 3×) unit.

Current and Voltage Data Acquisition

The current was measured with a LEM HTA 600-S current transducer, which has a current range of 0–600 A. An LEM LV25-P voltage transducer was used for voltage sampling; it is capable of sampling between 0 and 100 V. Both sensors were connected to a signal processing device. Figure 7 shows a representation of this setup.

Synchronization

Synchronization of the high-speed video with the high-speed current and voltage signals was accomplished using various techniques. Because the data card used in this research does not have analog output abilities, the signal had to first be routed through a digital relay. An AC voltage generator was then used to activate the mechanical relay that triggered the camera. The camera was triggered upon activation of the current and voltage acquisition system.

To synchronize the independent systems, an LED that operates off of the current/voltage system was placed in the line of sight of the camera. Programmed to activate every 100 ms for 10 ms, the LED allows for adjustment of the video to align with the current/voltage output. When the adjustment is complete, the video lags the current and voltage signals by approximately 1 ms. The video will always lag the current and voltage because of the delay in the mechanical relay used to activate the camera.

Figure 8 shows two images captured 10 ms apart. The vertical bar on the voltage readout indicates where the frame of the video aligns with the voltage signal. The videos were compiled by a MATLAB code written specifically for this project.

Results and Discussion

Droplet Heat Fraction

An advantage to using the current setup is the ability to separate the heat

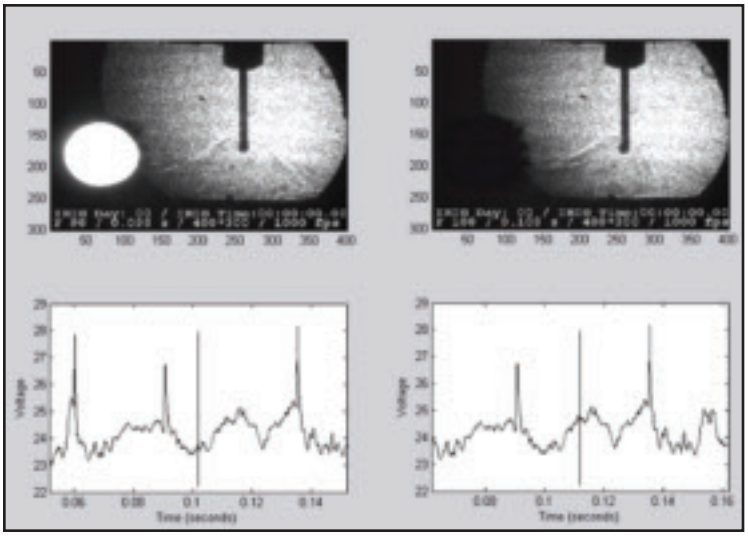

Fig. 8 — Images captured 10 ms apart using the synchronization system. This figure demonstrates the delay between the video and voltage signal. Although it was proven that the peaks correspond to droplet detachment (Ref. 18), the signal does not precisely correlate to the video. ER4043, 107 A.

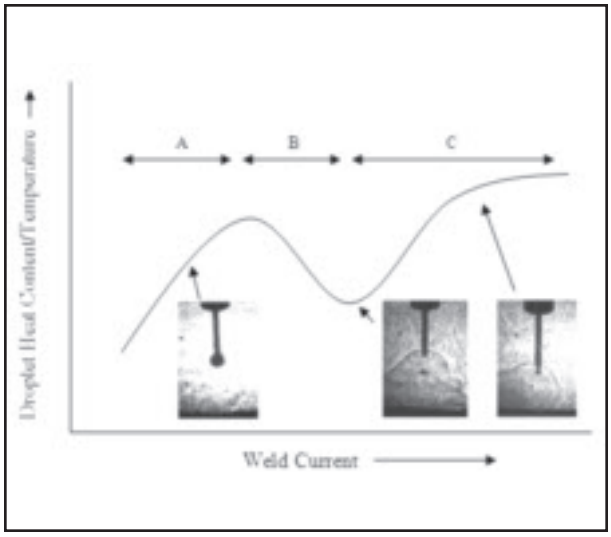

Fig. 9 — Generic trend seen in each case, with three distinct regions representing the following: A — Globular transfer; B — the transition region; C — spray transfer. The photographs are of 1.1-mm (0.045-in.) ER4043 electrodes shielded with argon.

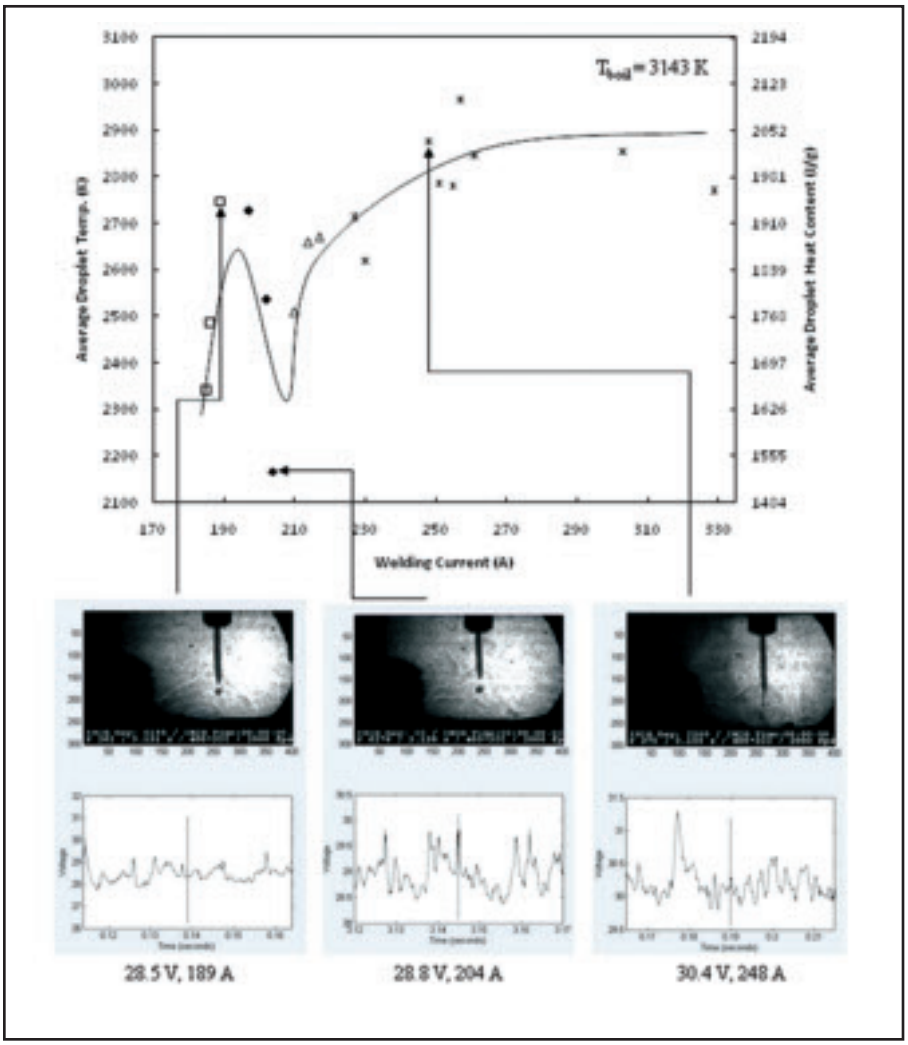

Fig. 10 — Average droplet temperature and average droplet heat content for ER70S-6 (mild steel) 1.1-mm (0.045-in.) electrodes shielded with argon. Data used for calculating average droplet temperature and heat content in regions A, B, and C are indicated by square, diamond, and triangle markers, respectively.

content of the droplets from that of the arc. Results from previous researchers show efficiencies anywhere from 68 to 88% (Refs. 7, 20–22), depending on the welding conditions. These results were found using a variety of methods, none of which isolates the arc from the droplets. The methodology for computing the heat fraction of the droplets is straightforward. The process is not completely efficient due to radiation and evaporative losses; therefore, for the nonpulsed conditions used, the total heat into the weld is given by the following:

$$q_w = IV\eta \qquad (1)$$

where q_w is the total energy input to the weld and η is the process efficiency. The main emphasis of this study is to determine the heat content of the droplets in globular and spray transfer modes, given by Equation 2:

$$q_d = f_d q_w \qquad (2)$$

where q_d is the heat contained within the droplets and f_d the droplet heat fraction. Both welding current and voltage were measured using transducers; therefore, the total power delivered to the system was calculated using Equation 1. Because the arc is separated from the calorimeter by the heat shield and copper cathode, any subsequent increase in the temperature of the water bath is considered to come from the droplets. Therefore, f_d is expressed by rearranging Equation 2, leaving

$$f_d = \frac{q_d}{q_w} \qquad (3)$$

Combining Equations 1 and 2 leaves the

total heat of the droplets in terms of the welding current, voltage, process efficiency, and droplet heat fraction as follows:

$$q_d = f_d \eta I V \quad (4)$$

Droplet Heat Content and Temperature

The behavior of both the average droplet heat content and average droplet temperature as a function of welding current followed the same generic trend for each of the alloys, shown in Fig. 9, with three distinct regions: A, corresponding to globular transfer mode; B, corresponding to the transition; and C, the region correlating to projected/streaming spray transfer. Droplet energy increased until the process reached a threshold, or the transition from globular to spray transfer. Although unstable, process operation within the transition region can help reduce fume formation and therefore alloy losses, two aspects that are highly desirable in industry when workplace cleanliness is of concern. Also, the advent of new, highly alloyed materials make reducing alloy losses necessary. This region can also be tailored using pulsing to make it more desirable for an industrial setting.

In the transition phase, droplet size decreased and the energy balance of the system changed. A detailed, theoretical study of this phenomenon is in progress. Intuitively, however, it is reasonable to expect that for a given droplet size, surface temperature increases with heat input which increases with current (Ref. 23). The sudden reduction of droplet size hinders development of the thermal gradient and therefore decreases average droplet temperature.

Heat content and droplet temperature are monotonically related through the specific heat capacity of the metal, and are calculated via a simple heat balance between the melting and superheating of the droplet and the calorimeter, as shown in Equation 5:

$$\int_{T_l}^{T_d} C_{pl} dT + \Delta H_f + \int_{T_f}^{T_s} C_{ps} dT = \int_{T_w}^{T_f} C_{pw} dT + \int_{T_w}^{T_f} C_{pc} dT \quad (5)$$

where T_d is the maximum temperature of the molten droplet, T_l is the liquidus temperature of the droplet, C_{ps} is the specific heat capacity of the solid metal, ΔH_f is the latent heat of fusion of the metal, T_s is the solidus temperature of the metal, T_f is the final temperature of the water in the calorimeter, C_{pl} is the specific heat capacity of the molten metal, T_w is the initial temperature in the water bath, C_{pw} is the specific heat of water, and C_{pw} is the specific heat of the copper crucible. In this first implementation of the calorimeter, average C_p values were used, resulting in the linear Equation 6. This equation can be easily solved, unlike Equation 5, which is nonlinear. More information about the values used in the calculation can be found in Appendix B.

$$C_{pl}(T_d - T_l) + \Delta H_f + C_{ps}(T_s - T_f) = C_{pw}(T_f - T_w) + C_{pc}(T_f - T_w) \quad (6)$$

In Equation 6, the only unknown is T_d, the temperature of the droplet after leaving the arc column. The approximation that C_p does not change significantly with temperature was made to simplify the calculations in this study. The authors acknowledge the influence of temperature on the heat capacity of materials, and are currently working on incorporating this variability into the calculations.

The average droplet temperature for each alloy is shown in Figs. 10–12. In these graphs, the points represent the experimental data, while the continuous lines represent a manual interpretation. Not all the data were of the same quality, in particular the case of the steel electrode for which the design of the cathode was still at an iteration stage, resulting in a relatively large scatter in Fig. 10.

An interesting observation should be noted. In the case of the steel electrode, the maximum recorded average droplet temperature is below the boiling temperature of the liquid. However, previous research has indicated temperatures at the surface of the droplet to be at the boiling point (Ref. 24). This suggests that the bulk temperature of the droplet is well below the boiling point of steel, and that vapor-

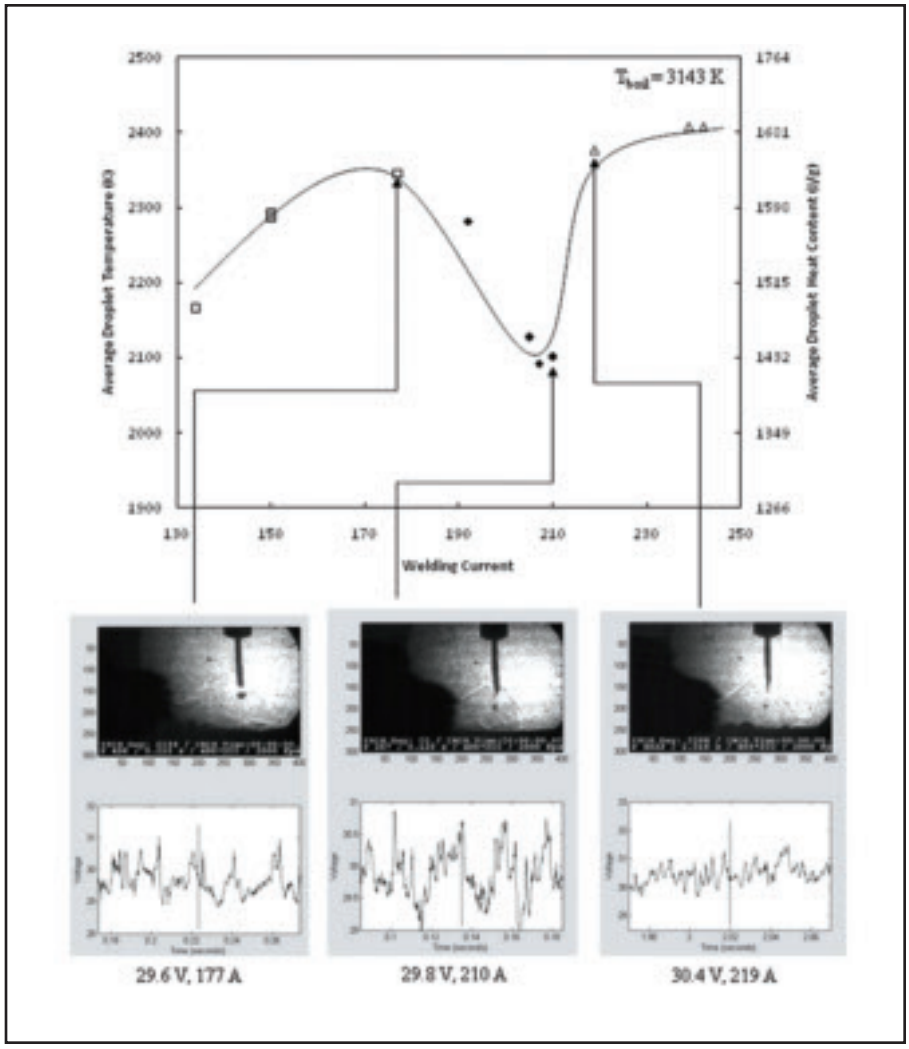

Fig. 11 — Average droplet temperature and average droplet heat content for 1.1-mm (0.045-in.) ER316L (316 stainless steel) electrodes shielded with argon. Data used for calculating average droplet temperature and heat content in regions A, B, and C are indicated by square, diamond, and triangle markers, respectively.

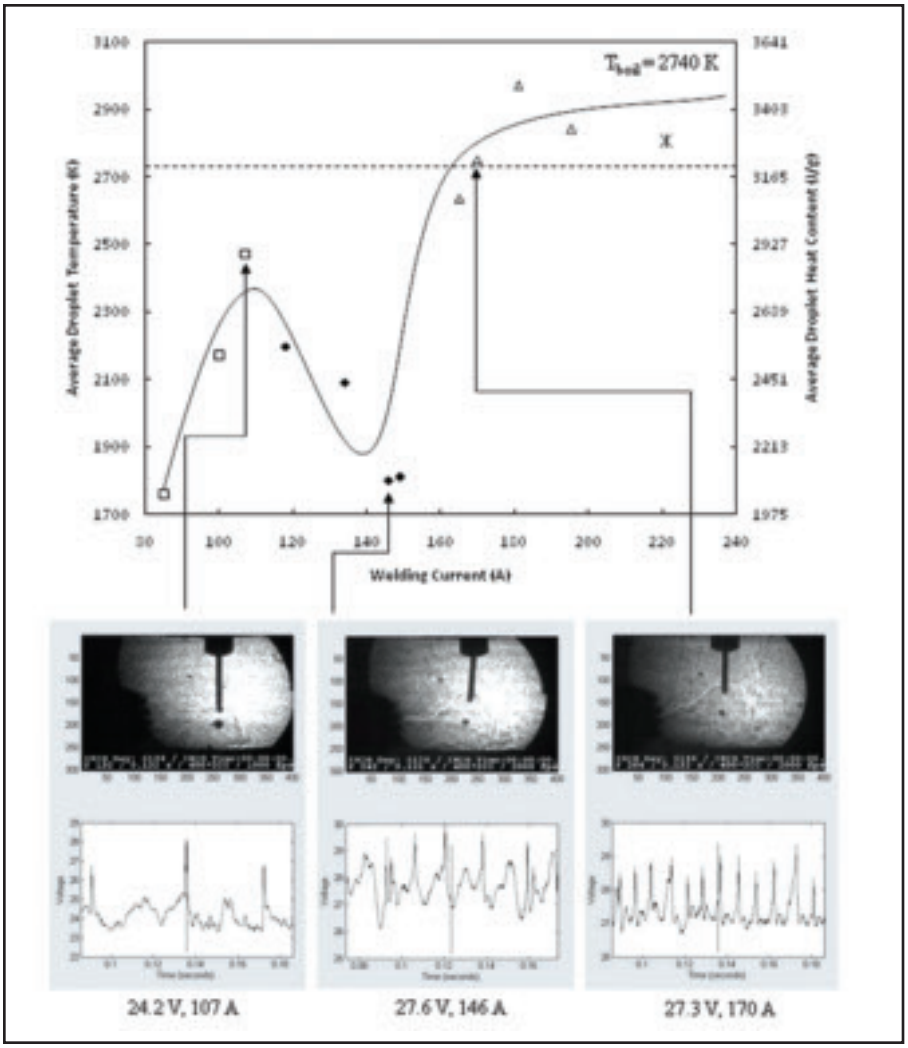

Fig. 12 — Average droplet temperature and average droplet heat content for 1.1-mm (0.045-in.) ER4043 (aluminum) electrodes shielded with argon. Data used for calculating average droplet temperature and heat content in regions A, B, and C are indicated by square, diamond, and triangle markers, respectively.

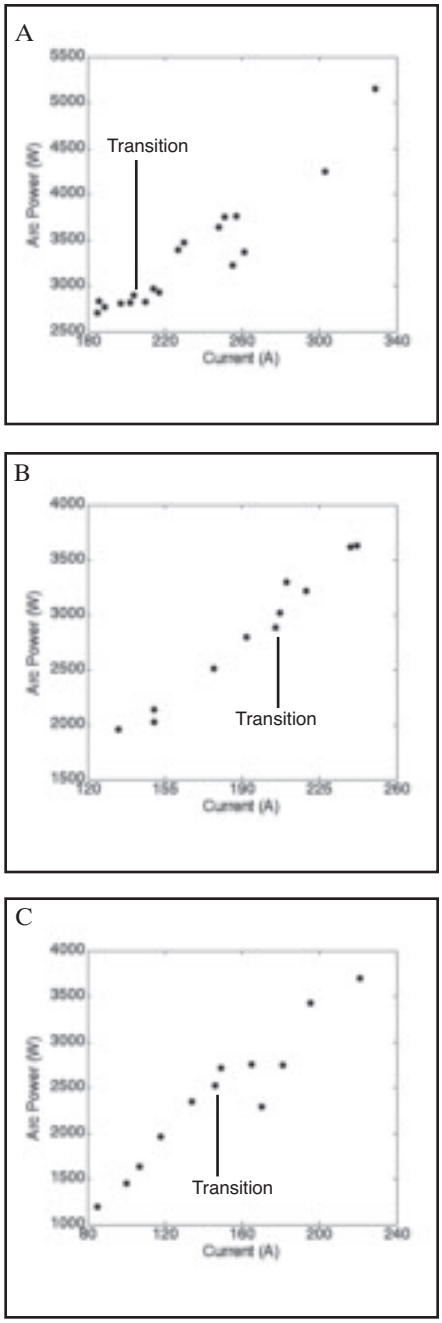

Fig. 13 — Cathodic heat input for the following: A — ER70S-6; B — ER316L; C — ER4043 1.1-mm (0.045-in.) electrodes shielded with argon.

ization may not be a dominant heat transfer mechanism. The same cannot be said for the aluminum droplets, however. The maximum recorded droplet temperature in this case was above the boiling point, indicating vaporization is a dominant heat transfer mechanism. In making these considerations, it is important to keep in mind that temperature gradients within the droplet can cause surface temperatures to be much higher than bulk temperatures.

Arc Power

The minimum seen in the droplet heat content was only seen in the droplets, and did not translate to the arc. Figure 13 shows a linear trend between arc power and welding current, as expected.

The apparent minimum arc power seen in the ER4043 data set, as well as the scatter seen in the ER70S-6 data set do not correspond to a minimum droplet temperature or any significant change with the process. They are likely related to experimental error.

Heat Distribution

Table 1 shows how heat is distributed between the electrode and cathode during welding on a copper cathode. For the constant voltage conditions used, average power input is calculated by multiplying the average welding current by the average voltage. Average droplet, cathodic, heat shield, and other heat fractions are calculated by dividing average droplet heat content, energy delivered to the cathode or heat shield and energy not directly measured by the total average power input. Average droplet heat content is calculated from Equation 6, from which average droplet temperature can be directly calculated. The calculation of process efficiency considers only the average droplet heat content and heat delivered to the cathode divided by average total power. Because radiation from the arc as well as from the plume extending below the cathode were not taken into account in the captured fraction calculation, the overall captured energy was lower than typical reported efficiency values.

The copper heat shield was not used consistently during the testing of the ER70S-6 electrodes and was therefore omitted from the table. In both ER316L and ER4043, the fraction of heat contained within the heat shield was quite low, between 5 and 11%. This suggests one of two things: either welding times were not long enough to allow the plate to come

to thermal equilibrium, or it is simply not capturing significant quantities of heat from the plasma flame. Changes can be made to the experimental procedure to determine the best way to capture more of the radiant heat.

Conclusion

- An experimental platform was constructed that has the ability to characterize several different aspects of the GMAW process. Metal transfer modes were analyzed with a high-speed laser imaging system that is synchronized to the current and voltage signal. The results show direct correlation between droplet detachment events and sharp peaks in the voltage outputs of the process. Energy measurements of both the detached droplets and welding arc were made on three separate calorimeter systems.

- Three different electrode materials, ER70S-6 steel, ER316L stainless steel, and ER4043 aluminum were tested for average droplet heat content and temperature during different metal transfer modes. The same trend was seen for all three alloys; a significant reduction in droplet heat content and average droplet temperature occurs at the transition from globular to spray transfer. Average droplet temperature increased slightly during globular transfer, was minimum at the transition between globular and spray transfer, and any subsequent increase in welding current in the spray transfer mode increased the heat content of the droplets.

Table 1 — Summary of Heat Distribution on ER70S-6, ER316L, and ER4043 Electrodes for the Three Transfer Modes Observed[(a)]

	Unit	A	B	C
ER70S-6				
Avg Power Input	W	5444	5835	5926
Avg Droplet	%	23	23	28
Avg Cathode	%	51	49	49
Avg Heat Shield	%	N/A	N/A	N/A
Losses Not Captured	%	26	28	22
Avg Droplet Temp.	K	2524	2476	2612
Avg Droplet Heat Content	J/g	1789	1753	1846
Captured Fraction	%	74	72	78
ER316L				
	Unit	A	B	C
Avg Power Input	W	4370	5947	7141
Avg Droplet	%	24	24	26
Avg Cathode	%	43	45	42
Avg Heat Shield	%	7	6	6
Losses Not Captured	%	27	25	25
Avg Droplet Temp	K	2273	2151	2397
Avg Droplet Content	J/g	1578	1474	1677
Captured Fraction	%	67	69	68
ER4043				
	Unit	A	B	C
Avg Power Input	W	2368	3625	4959
Avg Droplet	%	19	15	21
Avg Cathode	%	55	55	51
Avg Heat Shield	%	5	11	5
Losses Not Captured	%	21	19	23
Avg Droplet Temp.	K	2133	1975	2800
Avg Droplet Heat Content	J/g	2495	2305	3281
Captured Fraction	%	74	70	72

(a) Average values are tabulated by using points that lie closest to the transition, i.e., data collected at relatively high or low welding currents are neglected. The overall captured fraction is comparable to low values of efficiencies reported in literature. This suggests the setup does not lose much energy that would have been transferred to a substrate in typical bead-on-plate welding.

Acknowledgments

E. J. Soderstrom's work was funded by a graduate research fellowship from the AWS Foundation and support from Miller/ITW. K. M. Scott's work was supported by the AWS Arsham Amirikian Engineering Scholarship and the Natural Sciences and Engineering Research Council of Canada, Discovery grant no. 372104-09. The experimental work presented was performed at the CWJCR at Colorado School of Mines with support of the NSF CAREER award DMI-0547649. The authors also acknowledge valuable feedback from Bruce Albrecht and Rick Hutchison from Miller/ITW and MATLAB programming help from Andy Roubidoux.

References

1. Halmoy, E. 1979. Wire melting rate, droplet temperature, and effective anode melting potential. *Arc Physics and Weld Pool Behaviour*. London, UK: The Welding Institute.

2. Acinger, K., Sipek, L., and Smars, E. 1970. *Temperature, Metal Vapour Density and Energy Balance in an Argon Shielded Welding Arc with Iron Electrodes*, REP-70-10, editor. Electron Physics Division: Stockholm, Sweden.

3. Pintard, J. 1965. Contribution to research on metal transfer in MIG welding. *Soud. Techn. Conn.*

4. Pokhodnya, I. K., and Suptel, A. M. 1967. The heat contents of the droplets of electrode metal in gas shielded arc welding. *Avtomat. Svarka* 1967(2): 16–24.

5. Jelmorini, G., Tichelaar, G. W., and Van den Heuvel, G. J. P. M. 1977. *Droplet Temperature Measurements in Arc Welding.* IIW Document 212-411-77.

6. Lu, M. J., and Kou, S. 1989. Power inputs in gas metal arc welding of aluminum — Part 1. *Welding Journal* 68(9): 382-s to 388-s.

7. Lu, M. J., and Kou, S. 1989. Power inputs in gas metal arc welding of aluminum — Part 2. *Welding Journal* 68(11): 452-s to 456-s.

8. Ozawa, M., and Morita, T. 1963. The measurement of heat quantity in melted metals. *Journal of the Japan Welding Society* 32(2): 52–59.

9. Fu, X.-S., Ushio, M., and Matsuda, F. 1983. Melting characteristics of some steel and aluminum alloy wires in GMA welding. *Transactions of JWRI* 12(1): 167–173.

10. Kiyohara, M., Yamamoto, H., and Harada, S. 1979. Melting characteristics of a wire electrode in the MIG-welding of aluminum. *Arc Physics and Weld Pool Behaviour.* London, UK: The Welding Institute.

11. Ando, K., and Nishuguchi, K. 1968. *Mechanism of formation of pencil-point-like wire tip in GMA arc welding.* Int. Inst. Weld. Doc. IIW 212-156-68.

12. Erohin, A. A., and Rykalin, N. N. 1962. Heat balance of electrode droplet melting in arc welding. *Physics of the Welding Arc.* London, UK: The Institute of Welding.

13. Watkins, A. D. 1988. Heat transfer efficiency in gas metal arc welding. MS thesis, University of Idaho, Moscow, Idaho.

14. Pokhodnya, I. K., and Suptel, A. M. 1970. The heat content of droplets of electrode metal in CO_2 welding. *Avtomat. Svarka* 1970(10): 6–8.

15. Heiro, H., and North, T. H. 1976. The influence of welding parameters on droplet temperature during pulsed arc welding. *Welding and Metal Fabrication* 44(7): 482–485.

16. Ueguri, S., Hara, K., and Komura, H. 1985. Study of metal transfer in pulsed GMA welding. *Welding Journal* 64(8): 242-s to 250-s.

17. Tong, H., et al. 2005. Mechanism of welding fume suppression during AC-pulsed MIG welding of Al-Mg alloys. *Welding International* 19(7): 509–523.

18. Soderstrom, E. 2009. Gas metal arc welding electrode heat and mass transfer mechanisms. *Metallurgical and Materials Engineering*, P. F. Mendez, editor. Colorado School of Mines,

Golden, Colo.
19. Allemand, C. D., et al. 1985. A method of filming metal transfer in welding arcs. *Welding Journal* 64(1): 45–47.
20. DuPont, J. N., and Marder, A. R. 1995. Thermal efficiency of arc welding processes. *Welding Journal* 74(12): 406-s to 416-s.
21. Essers, W. G., and Walter, R. 1981. Heat transfer and penetration mechanism with GMA and plasma-GMA welding. *Welding Journal* 60(2): 37-s to 42-s.
22. Watkins, A. D. 1988. *Heat Transfer Efficiency in Gas Metal Arc Welding.* University of Idaho, Moscow, Idaho.
23. Waszink, J. H., and Van den Heuvel, G. J. P. M. 1982. Heat generation and heat flow in the filler metal in GMA welding. *Welding Journal* 61(8): 269-s to 282-s.
24. Villeminot, P. 1967. Argon MIG welding of mild steel, thermal study of the stick-out, transfer temperature (in French). *Conference Proceedings of Soud. Techn. Conn.* 21(9-10): 367–380.

Appendix A

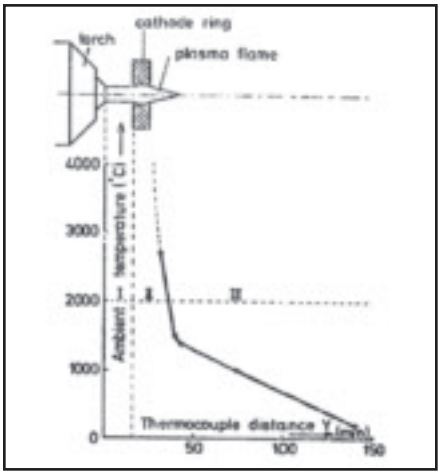

Fig. 14 — Ambient temperature readings using a thermocouple at different distances from a cathode ring. At approximately 140 mm (5.5 in.), the plasma flame shows little effect. From Jelmorini (Ref. 5).

In research conducted by Jelmorini (Ref. 5), it was shown that excess energy input from the plasma to the calorimeter may be problematic. To avoid excess heating, it was determined that the calorimeter should be ~140 mm (5.5 in.) below the exit of the cathode (Ref. 5). Figure 14 shows the results obtained by Jelmorini. In addition to the offset distance recommended by Jelmorini, this study used a copper heat shield to further reduce arc influence on the droplets and calorimeter.

Appendix B

See Table 2.

Appendix C

Procedure

- The power supply was turned on and shielding gas was purged through the system to ensure proper flow rate.
- Wire adjustment can be checked with a simple test of hand feeding the wire through the cable with little resistance.
- If new welding parameters are to be used, the proper adjustments (wire feed speed, voltage) need to be made prior to taking actual heat measurements. Adjustments are made to keep the contact tip to work distance and electrode extension constant at 25.4 mm (1 in.) and 12.7 mm (0.5 in.), respectively.
- Align the torch with the copper cathode by feeding enough wire through the contact tip such that it sticks through the hole in the cathode. Adjustments are made via X-Y-Z adjustment knobs.
- Clean the copper cathode using a die grinder equipped with a 76-mm-(3-in.-) diameter Scotch-Brite™ SL surface-conditioning disc.
- Set the process water flow rate to 3 L/min (0.79 gal/min) using the flow meter and ball valve on the copper cathode.
- Assemble the calorimeter. Prior to assembly, the Styrofoam and empty copper crucible are weighed individually to calculate any mass loss or gains during the experiment.
- The two thermocouples that monitor the temperature of the water bath are clamped into position with metal binder clips such that they are directly adjacent, but not touching, the copper crucible.
- Pour approximately 500 mL of water directly into the center cavity of the Styrofoam. Record the exact amount of water that is poured into the Styrofoam for later calculations. A magnetic stir bar is placed into the Styrofoam container, which is subsequently placed on the magnetic stirrer.
- Turn the magnetic stirrer to 400 rev/min.
- The calorimeter is now ready for the experiment. Raise the calorimeter to immerse the crucible in the water bath.
- The data acquired during experiments are divided into three separate categories: current and voltage, temperature, and video. All three are controlled by a program written in LabView.
- When all of the subassemblies are prepared for an experiment, the welding process can be enabled. The arc is started by using a flattened piece of copper tubing, positioned in such a way to create a short circuit between the wire and cathode.
- Once the process stabilizes, the manual trigger on the voltage/current acquisition can be pressed. This operation will simultaneously begin the voltage/current analysis as well as the high-speed video recording.
- Record the final weight of the Styrofoam container and copper crucible.
- Three different computer files are generated: the current/voltage signal, the temperature signal, and the movie file. These files are analyzed along with the weight and time measurements to determine average droplet detachment frequencies, heat contents, current, and voltage.

Table 2 — Thermophysical Properties of Materials Used in This Study (Ref. 24)

Material Property	Symbol	Unit	ER70S-6	ER316L	ER4043	Copper	Water
Liquid heat capacity	C_{pl}	J/gK	0.711	0.83	1.19		4.186
Solid heat capacity	C_{ps}	J/gK	0.685	0.6	1	0.385	
Heat of fusion	ΔH_f	J/g	250	260	425		
Liquidus temperature	T_l	K	1538	1402	614		
Solidus temperature	T_s	K	1538	1402[a]	614[a]		

(a) Although these alloys undergo a range of solidification, for the sake of the calculations, it was assumed that the solidus and liquidus temperatures are the same.